## PAPER

# Synthesis and engineering porosity of a mixed metal Fe₂Ni MIL-88B metal–organic framework†

Gia-Thanh Vuong, Minh-Hao Pham and Trong-On Do*

A new rational approach has been developed for the synthesis of a mixed metal MIL-88B metal–organic framework based on a neutral mixed metal cluster, such as Fe₂Ni(μ₃-O). Unlike the conventional negative charged single metal cluster, the use of the neutral mixed metal cluster as nodes in the framework avoids the need of a compensating anion inside the porous MIL-88B system; thus the mixed metal MIL-88B becomes porous. The flexibility of the mixed metal MIL-88B can be controlled by terminal ligands with different steric hindrance. This allows us to reversibly customize the porosity of the MIL-88B structure at three levels of specific surface area as well as the pore volume.

## Introduction

MOFs (metal–organic frameworks) are ordered structures of metal clusters connected by organic linkers.[1] This combination of an inorganic entity and an organic one can result in highly porous MOF crystals which show promising applications in adsorption, catalysis and drug delivery.[2–6] A classic example is the combination of trimeric $M_3(\mu_3\text{-O})$ clusters (M = Fe, Cr) with benzenedicarboxylate which gives rise to MIL-101, MIL-88B and MOF-235 structures of which only MIL-101 shows porosity.[7–13] As the metal is trivalent, a guest anion is needed to balance the charge of the cluster.[14] With regard to porosity, this anion is not desired. It blocks the pores, rendering the MOF structure non-porous as in the case of MIL-88B and MOF-235.[9,11] Only MIL-101 which has sufficiently large pore size can afford the high porosity.[10] In turn, the dense MIL-88B structure is not rigid but flexible, the network can expand upon adsorption of particular solvents. Such a great increase of 125% of unit cell volume can be obtained.[10,15] This distinctive feature coined the breathing effect by Férey *et al.* is of great interest since it provides facile control over the porosity by changing solvents.[10,15] Unfortunately, the flexibility of the MIL-88B structure is not permanent without solvent molecules. Solvent molecules must remain in its pores to sustain the expansion, hence despite a gain in pore size and pore volume, the pores are filled with solvent molecules and thus become inaccessible for adsorbates. Upon removal of solvents,
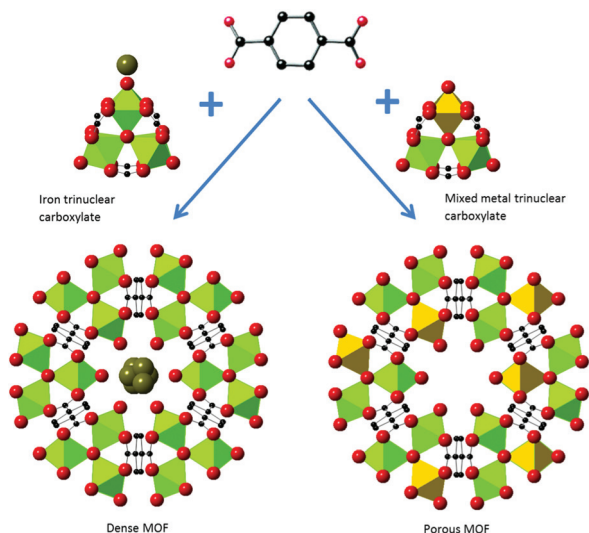
the structure shrinks, and MIL-88B returns to its dense state. A workaround to sustain the porosity of the MIL-88B structure has been recently reported.[16] Instead of the straight and simple linker benzenedicarboxylate, functional groups were introduced to the phenyl ring of the linker thus giving a steric hindrance effect to the linker. The obtained series of functionalized MIL-88B can resist the shrinkage, and one of them, MIL-88B(4CH₃), can yield specific areas up to 1200 m² g⁻¹.[16] However the reversibility of the breathing effect was not reported by the authors. And it is likely that the breathing magnitude in functionalized MIL-88B could become less due to the hindrance effect of the functional group, the structure is more likely "fixed".

On the other hand, most MOFs are based on single metals.[17,18] Many properties of MOFs are dependent on the metal component such as stability, magnetic behavior, density *etc.* Therefore, successful preparation of mixed metal MOFs would provide an effective way to fine tune the properties of MOFs. Direct syntheses of mixed metal MOFs are difficult, due to the high complexity upon addition of a second metal. Each metal can form separate clusters irrelevant and unconnected to the other metal clusters, resulting in a mixture of discrete MOFs. Rare-earth metals with high and flexible coordination capacity are able to join together with transition metals in some MOF structures.[19–21] However, this is not the case for main group and transition metals. The syntheses of mixed transition metal MOFs often employ linkers bearing free reactive functional groups that can coordinate with other metals in a pre- or post-synthesis treatment.[22–28] In this fashion, the second metal contributes nothing to the construction of the framework structure, but resides within it as an attachment. Few attempts which involve the selective introduction of the second metal have been reported to include both metals in the nodes of the framework. In these mixed metal MOFs, the

*Department of Chemical Engineering, Centre de Recherche sur les Interfaces et la Catalyse (CERPIC), Laval University, Quebec, G1V 0A6, Canada. E-mail: trong-on.do@gch.ulaval.ca*
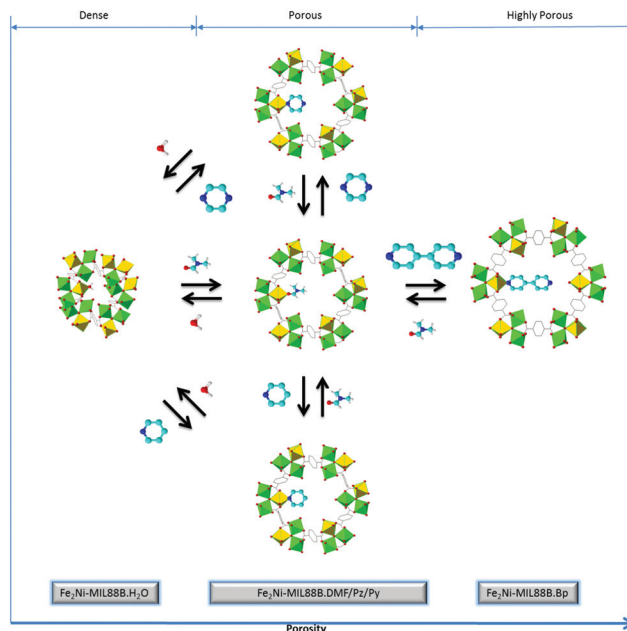
**Scheme 1** Mixed metal building unit forming porous MOF. Black: C; yellow: divalent metal (Ni); green: Fe; olive: balancing anion (Cl, Br *etc.*); red: O.



**Scheme 2** Reversible ligand exchange and porosity control of Fe$_2$Ni-MIL-88B, for clarity, only terminal ligands bonding to Ni are shown.

transition metal and the other one are distributed periodically among the nodes of the framework.[18]

Although mixed metal clusters such as trimeric metal carboxylates have been reported since 1911,[14,29] to the best of our knowledge there has been no report on MOF structures built on them. In fact, synthesis and characterization of trimeric mixed metal acetates of Fe(III) and first row divalent transition metals such as Co, Mn, Ni and Zn have been well established.[14] Thanks to the presence of the divalent metal, the mixed metal cluster is balanced in charge without a compensating anion. Judging from the similarity between the mixed metal cluster and the single metal cluster, we believe that it is possible to obtain analogs of those MOF structures such as MIL-101, MIL-88 from these mixed metal trimeric clusters. Because no compensating anion is needed in the framework, the pore blockage by anions is avoided, and the mixed metal MOF could become porous (Scheme 1).

In this paper, we report a new approach for the synthesis of mixed metal MIL-88B using a mixed metal cluster (Scheme 1) and the control of the breathing of the obtained mixed metal MOF *via* the steric hindrance of the terminal ligands (Scheme 2). To illustrate our approach, we have selected the synthesis of the MIL-88B structure based on the Fe$_2$Ni($\mu_3$-O) cluster (denoted as Fe$_2$Ni-MIL-88B). Our Fe$_2$Ni-MIL-88B product shows a drastic change over the original single metal Fe$_3$-MIL-88B in regard to porosity, and considerably high N$_2$ and CO$_2$ adsorption. But the most interesting feature of Fe$_2$Ni-MIL-88B is its switchable porosity and specific surface area (30 m$^2$ g$^{-1}$ to 1120 m$^2$ g$^{-1}$) and pore volume (10 × 10$^{-3}$ cm$^3$ g$^{-1}$ to 448 × 10$^{-3}$ cm$^3$ g$^{-1}$). Unlike the conventional single metal Fe$_3$-MIL-88B, Fe$_2$Ni-MIL-88B can switch reversibly and permanently from the dense state to the porous one upon ligand exchange with certain terminal ligands.

## Experiments

### Sample preparation

In a typical synthesis, 0.67 mmol of FeCl$_3$·6H$_2$O 99%, 0.33 mmol of corresponding Ni(NO$_3$)$_2$·6H$_2$O 97% and 1 mmol of bdc 98% were dissolved in 10 ml of DMF. To this clear solution, 0.4 mmol of NaOH was added under stirring for 15 min. The mixture was then transferred into a Teflon-lined autoclave and heated at 100 °C for 15 h. The solid product was then recovered by filtration and washed several times with DMF. Elemental analysis of the synthesized sample showed Fe 12.5 wt%, Ni 6.2 wt%, N 5.3 wt%. Thus, the suggested formula Fe$_2$NiO(OOC–C$_6$H$_4$–COO)$_3$·3DMF is designated as Fe$_2$Ni-MIL-88B·DMF. The sample was treated with water, pyridine (Py), pyrazine (Pz) and 4,4′-bipyridine (Bp) to obtain Fe$_2$Ni-MIL-88B·H$_2$O, Fe$_2$Ni-MIL-88B·Py, Fe$_2$Ni-MIL-88B·Pz and Fe$_2$Ni-MIL-88B·Bp, respectively (see ESI†). For comparison, the single metal Fe$_3$-MIL-88B·DMF was also prepared using the procedure of Férey *et al.*[30]

### Characterization

N$_2$ and CO$_2$ adsorption tests were carried out in an Autosorb 1 instrument, before analysis the samples were outgassed in a vacuum for 3 h at 150 °C. Specific surface area was calculated with the BET model in the linear range of $P/P_o$ = 0–0.15. FTIR was carried out in an FT-BIORAD 450s system using KBr discs. UV-VIS was carried out in a Cary 300 instrument using MgO discs. Powder X-ray diffraction (XRD) patterns were collected on a Bruker SMART APEX II X-ray diffractometer with Cu Kα radiation ($\lambda$ = 1.5406 Å) in the 2$\theta$ range of 1–50° at a scan rate of 1.0° min$^{-1}$. For XRD measurements of samples in Fig. 1 and for crystal lattice calculations, the samples were dried in a
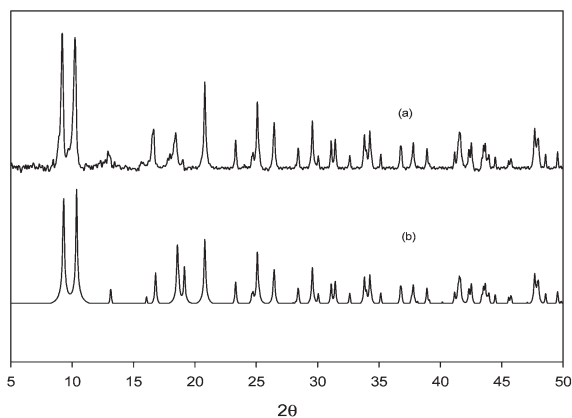
Fig. 1 XRD patterns of Fe$_2$Ni-MIL-88B·H$_2$O (a) and XRD simulation of Fe$_3$-MIL-88B (b).

vacuum overnight at 100 °C, then the analysis was taken immediately. Scanning electron microscopy (SEM) images were taken on a JEOL 6360 instrument at an accelerating voltage of 3 kV.

## Results

### Synthesis of mixed metal Fe$_2$Ni-MIL-88B with different terminal ligands

Details of the synthesis and ligand exchanges are described in the experimental section and in ESI.† Elemental analysis of the synthesized sample showed Fe 12.5 wt%, Ni 6.2 wt%, N 5.3 wt%. Thus, the suggested formula Fe$_2$NiO(OOC–C$_6$H$_4$–COO)$_3$·3DMF is designated as Fe$_2$Ni-MIL-88B·DMF. The sample was treated with water, pyridine (Py), pyrazine (Pz) and 4,4′-bipyridine (Bp) to obtain Fe$_2$Ni-MIL-88B·H$_2$O, Fe$_2$-MIL-88B·Py, Fe$_2$Ni-MIL-88B·Pz and Fe$_2$Ni-MIL-88B·Bp, respectively. For comparison, the pristine Fe$_3$-MIL-88B·DMF was also prepared using the procedure of Férey et al.[30]

The XRD patterns of all the Fe$_2$Ni-MIL-88B samples were collected, however, due to the flexibility of the MIL-88B structures, which will be explained in the next session, the best way to determine the structure of the samples is to compare the completely dense phase Fe$_2$Ni-MIL-88B·H$_2$O with the XRD simulation of the standard Fe$_3$-MIL-88B. As shown in Fig. 1,

the XRD of the Fe$_2$Ni-MIL-88B·H$_2$O is identical to the simulation one, in addition no guest phase is found, implying the MIL-88B structure with the high purity of the sample.

The FTIR analysis of the samples is in agreement with the suggested MIL-88B formula (for details, see Table 1 and Fig. S1–S6, ESI†). There are four remarks: (i) no free acid (no band at 1700 cm$^{-1}$) is found, (ii) the value $\Delta = \nu_{asym}(OCO) - \nu_{sym}(OCO)$ corresponds well to the bridge coordination mode of metal carboxylates,[31] (iii) the bands characteristic of H$_2$O, DMF, Py, Pz and Bp are present on the samples Fe$_2$Ni-MIL-88B·H$_2$O, Fe$_2$Ni-MIL-88B·DMF, Fe$_2$Ni-MIL-88B·Py, Fe$_2$Ni-MIL-88B·Pz and Fe$_2$Ni-MIL-88B·Bp, respectively, and (iv) the vibration of cluster Fe$_2$Ni($\mu_3$-O) (~718 cm$^{-1}$) is observed, while the vibration of Fe$_3$($\mu_3$-O) (620 cm$^{-1}$) is only noticed in the single metal Fe$_3$-MIL-88B sample.[37,38]

The UV-Vis spectra of the Fe$_2$Ni-MIL-88B samples with different terminal ligands are shown in Fig. 2. The UV-Vis analysis also confirms the presence of Ni as well as its octahedral coordination mode in the MIL-88B structures. The band at 244 nm is assigned to the ligand-to-metal charge transfer, implying the bonding of carboxylate oxygen to metal. Most of the transition bands of Ni$^{2+}$ are obscured by those of Fe$^{3+}$. However, the presence of the band at 760 nm which is characteristic of the transition [$^3$A$_{2g}$ => $^1$E$_g$(D)] of Ni in the trinuclear complex is observed. The transition [$^6$A$_{1g}$ => $^4$A$_{1g}$ + $^4$E$_g$(G)] in Fe$^{3+}$ is also found at 350–500 nm.[39,40] Especially, the [$^6$A$_{1g}$ => $^4$T$_{2g}$] transitions at 550–650 nm of Fe$^{3+}$, which are sensitive to the ligand field energy, clearly reveal the bonding of the terminal ligand to the metal and the effect of the divalent metal Ni in the complex. These transitions of the samples Fe$_2$Ni-MIL-88B·H$_2$O and Fe$_2$Ni-MIL-88B·DMF which involve the weak field terminal ligand H$_2$O and DMF are observed at 575 nm. Accordingly, for the samples involving the strong field ligands Py, Pz and Bp, these bands are shifted to lower energy (higher wavelength at 625 nm). This behavior is in agreement with the higher ligand field energy of Py, Pz, and Bp than that of H$_2$O and DMF.[40] In the Fe$_2$Ni complex under the effect of Ni, the ligand field in Fe reduces,[39] thus the [$^6$A$_{1g}$ => $^4$T$_{2g}$] transition in Fe$_3$-MIL-88B·DMF is at 525 nm while it is observed at 575 nm in the Fe$_2$Ni-MIL-88B·DMF. As seen in Fig. S7, ESI,† the change in color of the samples depends on the nature of the terminal ligand (a–d) as well as on the presence of Ni in the structure (d, f).

**Table 1** IR analysis of the MIL-88B samples

| Sample | $\nu_{asym}$(OCO) | $\nu_{sym}$(OCO) | $\Delta$[31][a] | DMF[32,33] | Py[34–36] | Pz[34] | Bp[35] | Fe$_2$NiO/Fe$_3$O[37,38] |
|---|---|---|---|---|---|---|---|---|
| | | | | | Wavenumber [cm$^{-1}$] | | | |
| Fe$_2$Ni-MIL-88B·Py | 1606 | 1382 | 224 | | 1486, 1447, 703, 633 | | | 718 |
| Fe$_2$Ni-MIL-88B·H$_2$O | 1590 | 1381 | 209 | | | | | 717 |
| Fe$_2$Ni-MIL-88B·DMF | 1609 | 1385 | 224 | 1660 | | | | 718 |
| Fe$_2$Ni-MIL-88B·Pz | 1603 | 1383 | 220 | | | 1416 | | 717 |
| Fe$_2$Ni -MIL-88B·Bp | 1609 | 1385 | 224 | | | | 1431, 1408, 635 | 718 |
| Fe$_3$-MIL-88B | 1601 | 1393 | 208 | 1666 | | | | 624 |

[a] $\Delta = \nu_{asym}(OCO) - \nu_{sym}(OCO)$.
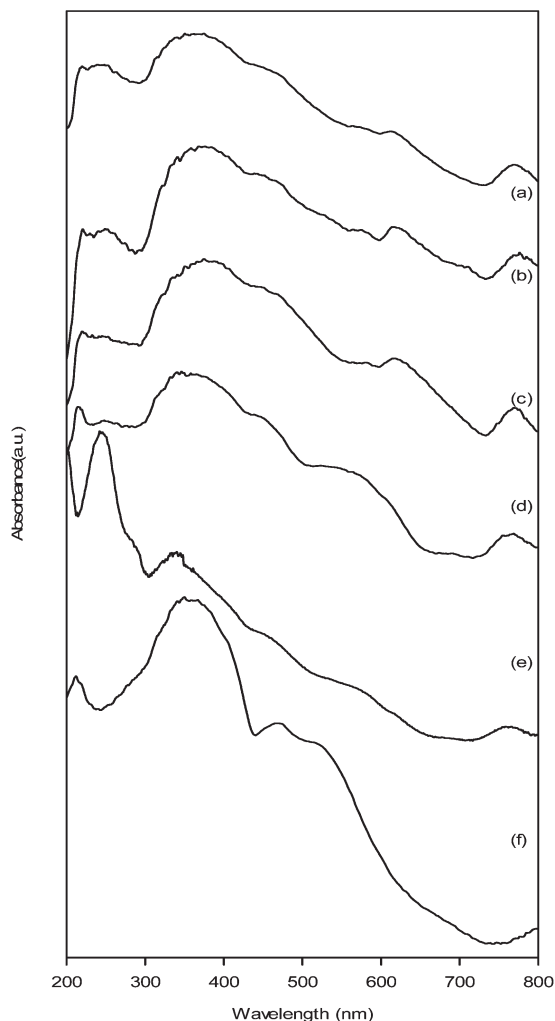
**Fig. 2** UV-Vis spectra of $Fe_2Ni$-MIL-88B·Bp (a), $Fe_2Ni$-MIL-88B·Pz (b), $Fe_2$Ni-MIL-88B·Py (c), $Fe_2Ni$-MIL-88B·DMF (d), $Fe_2Ni$-MIL-88B·$H_2O$ (e) and $Fe_3$-MIL-88B (f).
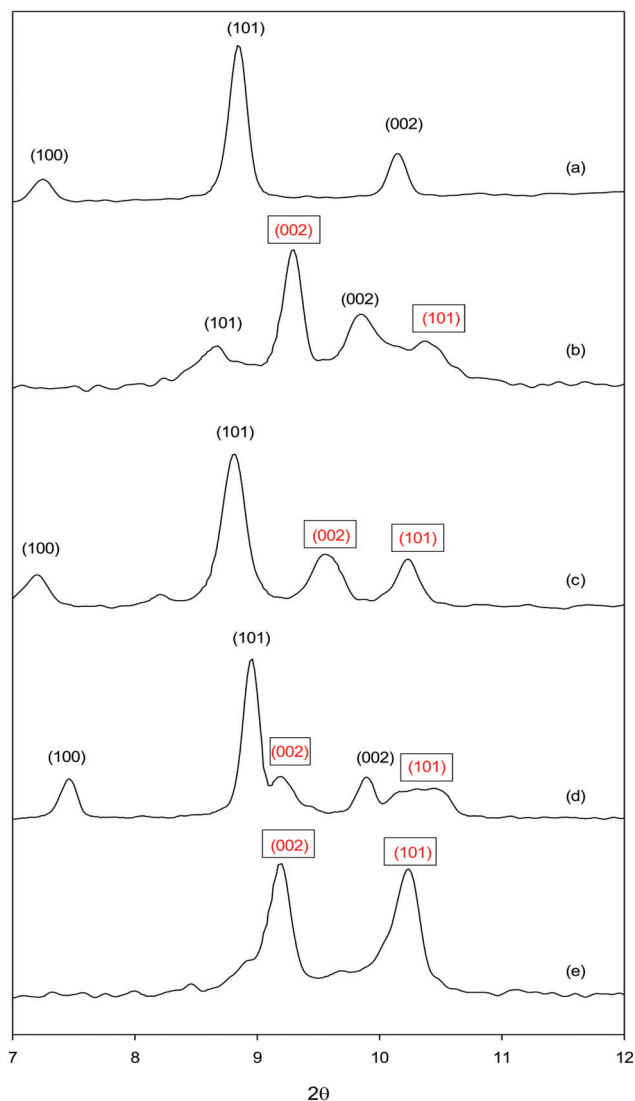


**Fig. 3** XRD patterns of $Fe_2Ni$-MIL-88B samples, the planes of the open phase are in black, the planes of the dense phase are in red and placed in boxes. $Fe_2Ni$-MIL-88B·Bp (a), $Fe_2Ni$-MIL-88B·Pz (b), $Fe_2Ni$-MIL-88B·Py (c), $Fe_2Ni$-MIL-88B·DMF (d) and $Fe_2Ni$-MIL-88B·$H_2O$ (e).

### Reversible breathing control using the terminal ligand

The breathing behavior of MIL-88B has been well documented by Férey *et al.*[8] and can be studied in detail by investigation of the XRD patterns in the $2\theta$ range from 7 to 12°. Fig. 3 shows the XRD patterns of the mixed metal samples with different terminal ligands, which also confirms the MIL-88B structure. For comparison the XRD pattern of $Fe_3$-MIL-88B is also displayed. As Férey *et al.* have reported,[8] the swelling up of the MIL-88B structure causes the splitting and shifting to low $2\theta$ of the planes (100) and (101), while the plane (002) is shifted to higher $2\theta$. Thus these planes can be used as the indicators of the swollen (open) phase as well as the dense phase in the samples. In Fig. 3, the planes assigned to the dense phase are in red and in boxes, while the ones assigned to the open phase are in black and without boxes. For the $Fe_2Ni$-MIL-88B·$H_2O$ sample, only the dense phase is observed. The $Fe_2Ni$-MIL-88B·DMF, $Fe_2Ni$-MIL-88B·Py and $Fe_2Ni$-MIL-88B·Pz samples feature both the open phase and the dense phase. The $Fe_2Ni$-MIL-88B·Bp sample exhibits an open structure

without any trace of the dense phase. Assuming the $Fe_2Ni$-MIL-88B samples taking the same hexagonal lattice structure as the original $Fe_3$-MIL-88B, calculations of the unit cell parameters using the assigned planes in Fig. 3 were carried out. The results listed in Table 2 are in agreement with the plane assignment. Upon swelling, the lattice constant $a$ increases from 11.0 Å to 14.4 Å while the $c$ constant decreases from 19.1 Å to 17.5 Å. Consequently, these changes are reflected in the unit cell volume. The unit cell volume of the open phase is about 40–50% higher than that of the dense phase. Obviously, the XRD patterns have demonstrated the effect of the terminal ligand on the swelling degree of the samples. In terms of steric hindrance, the terminal ligands can be classified into three groups: low hindrance of $H_2O$, intermediate of DMF, Py and Pz and high hindrance of Bp. The small ligand water with low steric hindrance hence cannot swell up the structure. In fact,

**Table 2** Crystal parameters of the $Fe_2Ni$-MIL-88B samples

| Sample | $a$ [Å] | $c$ [Å] | Unit cell volume [Å$^3$] | $\Delta V/V^a$ [%] |
|---|---|---|---|---|
| $Fe_2Ni$-MIL-88B·$H_2O$ | 11.2 | 19.1 | 2075 | — |
| $Fe_2Ni$-MIL-88B·DMF | | | | |
| —Open phase | 13.7 | 17.8 | 2893 | 39.4 |
| —Dense phase | 11.3 | 19.1 | 2112 | 1.8 |
| $Fe_2Ni$-MIL-88B·Py | | | | |
| —Open phase | 14.2 | 17.4 | 3039 | 46.4 |
| —Dense phase | 11.3 | 18.5 | 2046 | −1.4 |
| $Fe_2Ni$-MIL-88B·Pz | | | | |
| —Open phase | 14.4 | 17.8 | 3197 | 54.1 |
| —Dense phase | 11.0 | 19.0 | 1991 | −4.0 |
| $Fe_2Ni$-MIL-88B·Bp | 14.1 | 17.4 | 2996 | 44.4 |

$^a$ The increase in unit cell volume compared with the $Fe_2Ni$-MIL-88B·$H_2O$ sample.

the $Fe_2Ni$-MIL-88B·$H_2O$ sample exhibits a dense phase. The introduction of larger ligands DMF, Py and Pz with higher steric hindrance brings about the openness of the structure of the obtained $Fe_2Ni$-MIL-88B·DMF, $Fe_2Ni$-MIL-88B·Py and $Fe_2Ni$-MIL-88B·Pz samples, but the openness is not full yet as some of the dense phase still remains. The samples show both open and dense phases. Eventually, the ligand Bp, which has the largest size and steric hindrance among the terminal ligands used in this study, yields the fully opened $Fe_2Ni$-MIL-88B·Bp.

### Adsorption analysis

Fig. 4A shows the nitrogen adsorption isotherms of the $Fe_2Ni$-MIL-88B samples with different terminal ligands, which are also in agreement with the XRD results. All the isotherms of the $Fe_2Ni$-MIL-88B samples show the characteristics of microporous materials with the isotherm reaching a plateau at very low partial pressure. As the steric hindrance of the terminal ligand increases from the small size of water to the middle size of DMF, Py, Pz and finally to the large size of Bp, the BET specific surface area of the samples also exhibits three levels: (i) dense (non-porous to $N_2$), 30 m$^2$ g$^{-1}$ for $Fe_2Ni$-MIL-88B·$H_2O$; (ii) porous, 355–550 m$^2$ g$^{-1}$ for $Fe_2Ni$-MIL-88B·DMF, $Fe_2Ni$-MIL-88B·Py, $Fe_2Ni$-MIL-88B·Pz; and (iii) highly porous, 1120 m$^2$ g$^{-1}$ for $Fe_2Ni$-MIL-88B·Bp. The same trend for their micropore volumes is also observed, showing three levels of pore volume. If the micropore volume is taken as a factor measuring the breathing, then the pore volume of the $Fe_2Ni$-MIL-88B·Bp sample is about 44 times higher than that of the $Fe_2Ni$-MIL-88B·$H_2O$ sample. Interestingly, the micropore diameters calculated by the HK model[41] are also consistent with the steric hindrance of the corresponding terminal ligands (Fig. 4B). The $Fe_2Ni$-MIL-88B·Bp sample shows an average pore size of 6.3 Å, the highest value among the samples. The $Fe_2Ni$-MIL-88B·DMF, $Fe_2Ni$-MIL-88B·Py and $Fe_2Ni$-MIL-88B·Pz samples exhibit the value of 5.2 Å, while the pore volume of the dense structure $Fe_2Ni$-MIL-88B·$H_2O$ is negligible. Details of the porosity and the specific surface area of the samples are shown in Table 3.
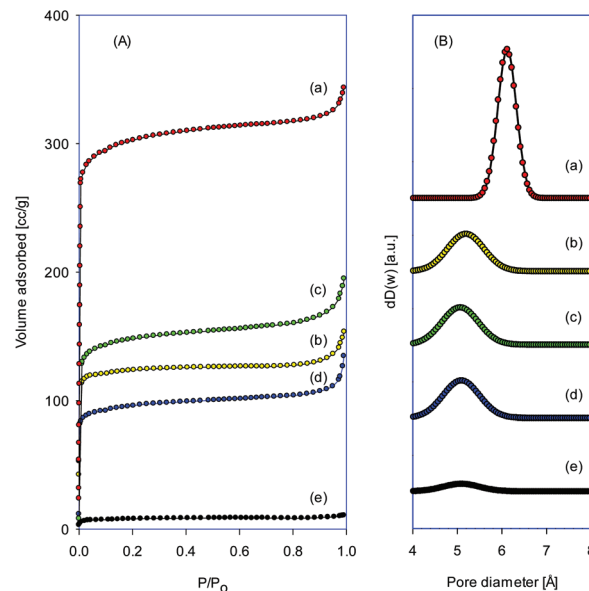


**Fig. 4** $N_2$ adsorption isotherms at 77 K (A) and pore size distributions (B) of $Fe_2Ni$-MIL-88B·Bp (a), $Fe_2Ni$-MIL-88B·Pz (b), $Fe_2Ni$-MIL-88B·Py (c), $Fe_2Ni$-MIL-88B·DMF (d) and $Fe_2Ni$-MIL-88B·$H_2O$ (e).

**Table 3** Porosity of $Fe_2Ni$-MIL-88B

| Samples | Specific surface area [m$^2$ g$^{-1}$] | Micropore volume [10$^{-3}$ cm$^3$ g$^{-1}$] | Pore width [Å] |
|---|---|---|---|
| $Fe_2Ni$-MIL-88B·$H_2O$ | 30 | 10 | — |
| $Fe_2Ni$-MIL-88B·DMF | 355 | 140 | 5.2 |
| $Fe_2Ni$-MIL-88B·Py | 549 | 216 | 5.2 |
| $Fe_2Ni$-MIL-88B·Pz | 465 | 186 | 5.2 |
| $Fe_2Ni$-MIL-88B·Bp | 1120 | 448 | 6.3 |

In addition to $N_2$ adsorption, the $CO_2$ adsorption measurements at low pressure (up to 1 atm) at 273 K were also carried out (Fig. 5). Again, the $CO_2$ adsorption capacity of the samples increases with the increase in porosity of the samples. The $Fe_2Ni$-MIL-88B·Bp sample shows the highest capacity, 101 cc g$^{-1}$ STP of $CO_2$, corresponding to a capacity of 20 wt%. This is one of the highest values (at 273 K at 1 atm) among MOF materials to date.[42] The high $CO_2$ adsorption capacity of $Fe_2Ni$-MIL-88B·Bp could be also due to the presence of the free pyridyl group of Bp in $Fe_2Ni$-MIL-88B·Bp, which has a high affinity with $CO_2$.

## Discussion

It is clear from the XRD analysis that our synthesized samples have the MIL-88B structure with high purity. Both FTIR and UV-Vis analyses and elemental analysis indicate the presence of Ni in the mixed metal MIL-88B samples. Interestingly, the spectroscopy techniques provide us with unambiguous evidence of the presence of the $Fe_2NiO$ cluster which is the building unit of the mixed metal MIL-88B. The presence of the $Fe_3O$ cluster which is the building unit of $Fe_3$-MIL-88B was not
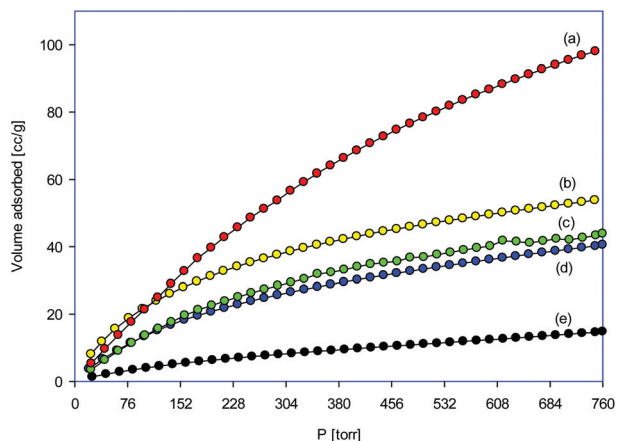
**Fig. 5** $CO_2$ adsorption isotherms at 273 K of $Fe_2Ni$-MIL-88B·Bp (a), $Fe_2Ni$-MIL-88B·Pz (b), $Fe_2Ni$-MIL-88B·Py (c), $Fe_2Ni$-MIL-88B·DMF (d) and $Fe_2Ni$-MIL-88B·$H_2O$ (e).

detected by FTIR and UV-Vis analyses of the mixed metal samples. Hence this suggests the mixed metal $Fe_2Ni$-MIL-88B structure.

Mixed metal $Fe_2Ni$-MIL-88B exhibits stable, controllable and permanent porosity, much better than single metal $Fe_3$-MIL-88B. The spectroscopy results revealed that the substituting ligands Py, Pz, and Bp are bound to the framework via a chemical bond to the metal atom, not physically packing. In fact, DMF, $H_2O$, Py, Pz and Bp are the terminal ligands in the $Fe_2NiO$ cluster. The XRD analysis and adsorption isotherm measurements of the samples $Fe_2Ni$-MIL-88B·$H_2O$, $Fe_2$-MIL-88B·DMF, $Fe_2Ni$-MIL-88B·Py, $Fe_2Ni$-MIL-88B·Pz and $Fe_2$-MIL-88B·Bp demonstrate that the porosity of the mixed metal $Fe_2Ni$-MIL-88B can be controlled by the size of the terminal ligands. Since the terminal ligand is chemically bonded to the metal rather than a weak physical packing, the impact is permanent. The samples retained their porosity after various types of treatment: drying in a vacuum at 150 °C for 24 h, and/ or exposure to air at room temperature for days. In contrast, this behavior was not observed on single metal $Fe_3$-MIL-88B treated with Py or Bp under the same conditions; no improvement in porosity was found on $Fe_3$-MIL-88B after the Py exchange. This drastic difference in the breathing behavior between $Fe_2Ni$-MIL-88B and the original $Fe_3$-MIL-88B stems from their different breathing mechanisms. While the breathing effect in $Fe_3$-MIL-88B originates from the packing of solvent molecules, this effect in $Fe_2Ni$-MIL-88B comes from the bonding of neutral ligands to the trinuclear clusters. The "swelling up" in $Fe_2Ni$-88B would be dependent on the size of the ligand and its orientation in bonding with the ligand. The larger the ligand is, the higher is the swelling up. And since bonding to each metal atom in the MIL-88B structure is a terminal ligand ($H_2O$ or DMF), which is ready to be replaced, it is possible to introduce larger terminal ligands into the MIL-88B structure which helps retain the breathing effect. Common terminal ligands for trimeric clusters are pyridine and its derivatives such as pyrazine and 4,4′-bipyridine,[14,43]

which have different steric hindrances and thus can be used as the breathing agent of the MIL-88B structure, as illustrated in Scheme 2.

It should be noted that for the original single metal $Fe_3$-MIL-88B, the activation conditions affect strongly the specific surface area. For example the badly activated $Fe_3$-MIL-88B ($CH_3$) solid that still contains some DMF exhibits a significant BET surface area while the fully water exchange sample is non-porous when dried.[16] This behaviour is attributed to the dependency of $Fe_3$-MIL-88B on the solvent to retain its porosity, as long as the solvent is present, the pores are opened. Thus the solvent molecule is the pore opening agent for $Fe_3$-MIL-88B. In the case of $Fe_2Ni$-MIL-88B it is the terminal ligand that keeps the pores open and since the terminal ligand is chemically bonded to the framework, it is expected that the porosity of $Fe_2Ni$-MIL-88B would be more stable. However, more quantitative work such as PXRD simulation will be necessary to confirm the mechanism of the pore opening in mixed metal MIL-88B.

For the rigid structure, addition of a guest molecule into the pores always results in a decrease in surface area; this is due to the fact that the guest molecule will partially block the pores, thus reducing the accessible surface. For example the attachment of a chiral organic ligand to $Cr_3$-MIL-101 reduces the surface area by 70%.[44] However this trend is reversed in mixed metal $Fe_2Ni$-MIL-88B, the larger the ligand is, the higher is the surface area obtained. It is the flexibility of the mixed metal $Fe_2Ni$-MIL-88B that gives this interesting behavior. As the XRD patterns show (Fig. 3), the large ligand can trigger the mixed metal $Fe_2Ni$-MIL-88B framework to expand further, opening the pores, thus gaining surface area.

The secondary divalent metal (Ni) in the mixed metal $Fe_2Ni$-MIL-88B is also very important to the obtained structure. As discussed earlier, the introduction of the divalent metal helps avoid the need of the blocking anions, in addition the bond strength of the cluster to the terminal ligand can be improved by selection of the second divalent metal which has higher affinity to the ligand. For the trimeric mixed metal $Fe_2^{III}M^{II}(\mu_3$-O)($\mu_2$-$O_2CCH_3$)$_6L_3$ with L being the pyridine derivative terminal ligand and M a divalent metal, Novitchi et al.[43] found that the stability of the Ni–L bond is 44 times higher than Fe–L; and Co–L is 6 times higher than Fe–L. Moreover, in a classic paper by Irving and Williams the stability constants of the pyridine-based $[M^{II}(Py)(H_2O)_5]^{2+}$ follow the order $Mn^{2+}(0.14) < Fe^{2+}(0.6) < Co^{2+}(1.14) < Ni^{2+}(1.78)$.[45] In fact, the improvement in stability of Ni-based complexes has been well established, thanks to the maximal crystal field stabilization energy of $Ni^{2+}$.[45] Hence, it is suggested that the mixed metal MOF based on the $Fe_2Ni(\mu_3$-O) cluster would exhibit stronger binding affinity to pyridine-like terminal ligands. Moreover, taking into account the anion-free state of the mixed metal MOF, the ligand can orient with less restriction inside the pores to attain a proper bond to the metal.

Besides the exceptional advantage of permanent porosity, the use of a terminal ligand as a swelling agent has another fascinating feature: reversibility. The terminal ligand is

exchangeable without affecting the linkers and the nodes of the framework. As illustrated in Scheme 2, the samples of Fe$_2$Ni-MIL-88B·DMF, Fe$_2$Ni-MIL-88B·H$_2$O, Fe$_2$Ni-MIL-88B·Py, and Fe$_2$Ni-MIL-88B·Pz can be mutually converted with the corresponding ligand exchange. The XRD and N$_2$ adsorption isotherm results show that the samples retain their crystallinity as well as porosity after the various conversion cycles. The Fe$_2$Ni-MIL-88B·Bp sample can be converted to Fe$_2$Ni-MIL-88B·DMF and then from this state it can be converted to bear any other ligand of Py, Pz, DMF and H$_2$O. This means that the porosity of Fe$_2$Ni-MIL-88B can be switched *in situ* to yield the necessary porosity, one of the desired features of smart porous materials.

Unlike zeolites and mesoporous inorganic materials regarded as rigid and fixed-pore structures, the reversible change in pore size of Fe$_2$Ni-MIL-88B is achieved by the breathing of the whole structure with the use of the terminal ligands to sustain it. Consequently, Fe$_2$Ni-MIL-88B can also provide at least three different states of porosity (Scheme 2). In fact, breathing can bring about a 300% change in volume in some MOFs. In addition, the terminal ligands are available in many sizes as well as the bond strength. Hence we believe the pore size control in MOFs is much easier and higher in magnitude and importantly not exclusive to Fe$_2$Ni-MIL-88B, but available to other MOFs capable of breathing.

Another general advantage of trimeric mixed metal is the ability to tether functional groups to the MOF structure. In this study, with the use of Pz and Bp, the free pyridyl group becomes available in the MIL-88B structure. It is very likely that other functional groups such as carboxyl and aldehyde can be introduced in the same manner using the corresponding ligands such as nicotinic acid and pyridinecarboxaldehyde. The key point about trimeric mixed metal MOFs is that the functional group can be prepared separately, and then attaches to the MOF structure as a removable module, the MOF hence becomes a flexible docking station for various types of functional modules.

## Conclusions

In the field of adsorption and membrane technologies, a smart material which can switch itself from high to low porosity or *vice versa* could be extremely beneficial. Imagine an adsorbent that can take in desired gas molecules with high capacity, but can also become inaccessible for them upon terminal ligand exchange; or a membrane that can let certain gas molecules pass through but can be shut off entirely to them if necessary. Many applications could benefit from this kind of "on and off" material.

We regard the Fe$_2$Ni-MIL-88B material as one step toward the creation of a truly smart porous material. Its versatility lies in its switchable and reversible three-level porosity. Different levels could be attained depending on the nature of the stimulant terminal ligand. Their obvious applications are of course adsorption and separation in which the pore size of the

material can be reversibly controlled to be wide opened, half opened or be completely closed at will.

In conclusion, we have succeeded in synthesizing the MIL-88B structure based on the mixed metal cluster of Fe(III) and Ni(II). This mixed metal cluster helps bring in porosity to the MOF product and exact control over the porosity and surface area by using simple stimulant terminal ligands. We believe that this rational approach is not restricted to the MIL-88B structure but can cover all the other flexible MOF structures which are based on trinuclear metal carboxylates MIL-101, MIL-100, MIL-88 and MOF-235 *etc.* With the rich choice of mixed metal clusters from a large collection of trimeric mixed metal clusters M$_2^{III}$M$^{II}$ (M$^{III}$: Fe, Cr, Mn, Rh and M$^{II}$: Ca, Ba, Mg, Ni, Mn, Co) and the great selection of terminal ligands among N-based, S-based, O-based ligands, there are immense opportunities for new fascinating properties of trimeric mixed metal MOFs.

## Acknowledgements

## Notes and references

1 O. M. Yaghi, M. O'Keeffe, N. W. Ockwig, H. K. Chae, M. Eddaoudi and J. Kim, *Nature*, 2003, **423**, 705–714.
2 A. Corma, H. García and F. X. Llabrés i Xamena, *Chem. Rev.*, 2010, **110**, 4606–4655.
3 J. Lee, O. K. Farha, J. Roberts, K. A. Scheidt, S. T. Nguyen and J. T. Hupp, *Chem. Soc. Rev.*, 2009, **38**, 1450–1459.
4 J.-R. Li, R. J. Kuppler and H.-C. Zhou, *Chem. Soc. Rev.*, 2009, **38**, 1477–1504.
5 L. J. Murray, M. Dinca and J. R. Long, *Chem. Soc. Rev.*, 2009, **38**, 1294–1314.
6 P. Horcajada, T. Chalati, C. Serre, B. Gillet, C. Sebrie, T. Baati, J. F. Eubank, D. Heurtaux, P. Clayette, C. Kreuz, J.-S. Chang, Y. K. Hwang, V. Marsaud, P.-N. Bories, L. Cynober, S. Gil, G. Ferey, P. Couvreur and R. Gref, *Nat. Mater.*, 2010, **9**, 172–178.
7 M.-H. Pham, G.-T. Vuong, A.-T. Vu and T.-O. Do, *Langmuir*, 2011, **27**, 15261–15267.
8 C. Serre, C. Mellot-Draznieks, S. Surble, N. Audebrand, Y. Filinchuk and G. Ferey, *Science*, 2007, **315**, 1828–1831.
9 S. Surble, C. Serre, C. Mellot-Draznieks, F. Millange and G. Ferey, *Chem. Commun.*, 2006, 284–286.
10 G. Ferey, C. Mellot-Draznieks, C. Serre, F. Millange, J. Dutour, S. Surble and I. Margiolaki, *Science*, 2005, **309**, 2040–2042.
11 A. C. Sudik, A. P. Côté and O. M. Yaghi, *Inorg. Chem.*, 2005, **44**, 2998–3000.

12 J. H. Yoon, S. B. Choi, Y. J. Oh, M. J. Seo, Y. H. Jhon, T.-B. Lee, D. Kim, S. H. Choi and J. Kim, *Catal. Today*, 2007, **120**, 324–329.

13 M.-H. Pham, G.-T. Vuong, F.-G. Fontaine and T.-O. Do, *Cryst. Growth Des.*, 2011, **12**, 1008–1013.

14 R. D. Cannon and R. P. White, *Prog. Inorg. Chem.*, John Wiley & Sons, Inc., 1988, vol. 36, pp. 195–298.

15 G. Ferey and C. Serre, *Chem. Soc. Rev.*, 2009, **38**, 1380–1399.

16 P. Horcajada, F. Salles, S. Wuttke, T. Devic, D. Heurtaux, G. Maurin, A. Vimont, M. Daturi, O. David, E. Magnier, N. Stock, Y. Filinchuk, D. Popov, C. Riekel, G. Férey and C. Serre, *J. Am. Chem. Soc.*, 2011, **133**, 17839–17847.

17 D. J. Tranchemontagne, J. L. Mendoza-Cortes, M. O'Keeffe and O. M. Yaghi, *Chem. Soc. Rev.*, 2009, **38**, 1257–1283.

18 S. R. Caskey and A. J. Matzger, *Inorg. Chem.*, 2008, **47**, 7942–7944.

19 B. Zhao, X.-Y. Chen, P. Cheng, D.-Z. Liao, S.-P. Yan and Z.-H. Jiang, *J. Am. Chem. Soc.*, 2004, **126**, 15394–15395.

20 B. Zhao, P. Cheng, Y. Dai, C. Cheng, D.-Z. Liao, S.-P. Yan, Z.-H. Jiang and G.-L. Wang, *Angew. Chem., Int. Ed.*, 2003, **42**, 934–936.

21 J.-W. Cheng, J. Zhang, S.-T. Zheng, M.-B. Zhang and G.-Y. Yang, *Angew. Chem., Int. Ed.*, 2006, **45**, 73–77.

22 E. D. Bloch, D. Britt, C. Lee, C. J. Doonan, F. J. Uribe-Romo, H. Furukawa, J. R. Long and O. M. Yaghi, *J. Am. Chem. Soc.*, 2010, **132**, 14382–14384.

23 S.-H. Cho, B. Ma, S. T. Nguyen, J. T. Hupp and T. E. Albrecht-Schmitt, *Chem. Commun.*, 2006, 2563–2565.

24 C. J. Doonan, W. Morris, H. Furukawa and O. M. Yaghi, *J. Am. Chem. Soc.*, 2009, **131**, 9492–9493.

25 S. J. Garibay, Z. Wang and S. M. Cohen, *Inorg. Chem.*, 2010, **49**, 8086–8091.

26 F. Song, C. Wang, J. M. Falkowski, L. Ma and W. Lin, *J. Am. Chem. Soc.*, 2010, **132**, 15390–15398.

27 K. C. Szeto, K. P. Lillerud, M. Tilset, M. Bjørgen, C. Prestipino, A. Zecchina, C. Lamberti and S. Bordiga, *J. Phys. Chem. B*, 2006, **110**, 21509–21520.

28 K. C. Szeto, C. Prestipino, C. Lamberti, A. Zecchina, S. Bordiga, M. Bjørgen, M. Tilset and K. P. Lillerud, *Chem. Mater.*, 2007, **19**, 211–220.

29 R. Weinland and H. Holtmeier, *Z. Anorg. Allg. Chem.*, 1928, **173**, 49–62.

30 S. Bauer, C. Serre, T. Devic, P. Horcajada, J. r. m. Marrot, G. r. Férey and N. Stock, *Inorg. Chem.*, 2008, **47**, 7568–7576.

31 U. Kumar, J. Thomas and N. Thirupathi, *Inorg. Chem.*, 2009, **49**, 62–72.

32 A. Fateeva, P. Horcajada, T. Devic, C. Serre, J. Marrot, J.-M. Grenèche, M. Morcrette, J.-M. Tarascon, G. Maurin and G. Férey, *Eur. J. Inorg. Chem.*, 2010, **2010**, 3789–3794.

33 Y. J. Kim and C. R. Park, *Inorg. Chem.*, 2002, **41**, 6211–6216.

34 M. I. Zaki, M. A. Hasan, F. A. Al-Sagheer and L. Pasupulety, *Colloids Surf., A*, 2001, **190**, 261–274.

35 K. Nakamoto, *Infrared and Raman Spectra of Inorganic and Coordination Compounds*, John Wiley & Sons, Inc., 2008, pp. 1–273.

36 K. N. Wong and S. D. Colson, *J. Mol. Spectrosc.*, 1984, **104**, 129–151.

37 M. Yazdanbakhsh, H. Tavakkoli, M. Taherzadeh and R. Boese, *J. Mol. Struct.*, 2010, **982**, 176–180.

38 L. Meesuk, U. A. Jayasooriya and R. D. Cannon, *Spectrochim. Acta, Part A*, 1987, **43**, 687–692.

39 A. B. Blake and A. Yavari, *J. Chem. Soc., Chem. Commun.*, 1982, 1247–1249.

40 A. B. Blake, A. Yavari, W. E. Hatfield and C. N. Sethulekshmi, *J. Chem. Soc., Dalton Trans.*, 1985, 2509–2520.

41 G. Horváth and K. Kawazoe, *J. Chem. Eng. Jpn.*, 1983, **16**, 470–475.

42 K. Sumida, D. L. Rogow, J. A. Mason, T. M. McDonald, E. D. Bloch, Z. R. Herm, T.-H. Bae and J. R. Long, *Chem. Rev.*, 2011, **112**, 724–781.

43 G. Novitchi, F. Riblet, R. Scopelliti, L. Helm, A. Gulea and A. E. Merbach, *Inorg. Chem.*, 2008, **47**, 10587–10599.

44 M. Banerjee, S. Das, M. Yoon, H. J. Choi, M. H. Hyun, S. M. Park, G. Seo and K. Kim, *J. Am. Chem. Soc.*, 2009, **131**, 7524–7525.

45 H. Irving and R. J. P. Williams, *J. Chem. Soc.*, 1953, 3192–3210.

# SUPPORTING INFORMATION

## Synthesis and Engineering Porosity of mixed metal Fe$_2$Ni MIL-88B Metal-Organic Framework

**Authors:** Gia-Thanh Vuong, Minh-Hao Pham, Trong-On Do*

**Affiliations:**

Department of Chemical Engineering, Centre de Recherche sur les Interfaces et la Catalyse (CERPIC), Laval University, Quebec, G1V 0A6, Canada

*Correspondence to: Trong-On.Do@gch.ulaval.ca.

## Preparation

In a typical synthesis, 0.67 mmol of $FeCl_3.6H_2O$ 99%, 0.33 mmol of corresponding $Ni(NO_3)_2.6H_2O$ 97% and 1 mmol of bdc 98% were dissolved in 10 ml of DMF. To this clear solution, 0.4 mmol of NaOH was added under stirring for 15 min. The mixture was then transferred into an Teflon-lined autoclave and heated at 100 $^o$C for 15 h. Solid product was then recovered by filtration and washed several times with DMF.

## Characterization

$N_2$ and $CO_2$ adsorption tests were carried out in an Autosorb 1 instrument, before analysis the samples were outgassed in vacuum for 3 hours at 150 $^o$C. Specific surface area was calculated with the BET model in the linear range of P/Po = 0 – 0.15.   KBr solid state FTIR was carried in a FT-BIORAD 450s system. MgO solid state UV-VIS was carried in a Cary 300 instrument. Powder X-ray diffraction (XRD) patterns were collected on a Bruker SMART APEX II X-ray diffractometer with Cu Kα radiation (λ = 1.5406 Å) in the 2θ range of 4 – 20° at a scan rate of 1.0° min$^{-1}$. For XRD measurement of samples in Figure 3 and for crystal lattice calculation, the samples were dried in vacuum overnight at 100 $^o$C, then the analysis was taken immediately. Peak fitting was carried out using Jade software package (http://www.materialsdata.com/).

Simulation of $Fe_3$-MIL-88B XRD pattern was done on the crystalography data reported by Férey et al [1] using Mercury software package (https://www.ccdc.cam.ac.uk/products/mercury/)

Scanning electron microscopy (SEM) images were taken on a JEOL 6360 instrument at accelerating voltage of 3 kV

**FTIR**
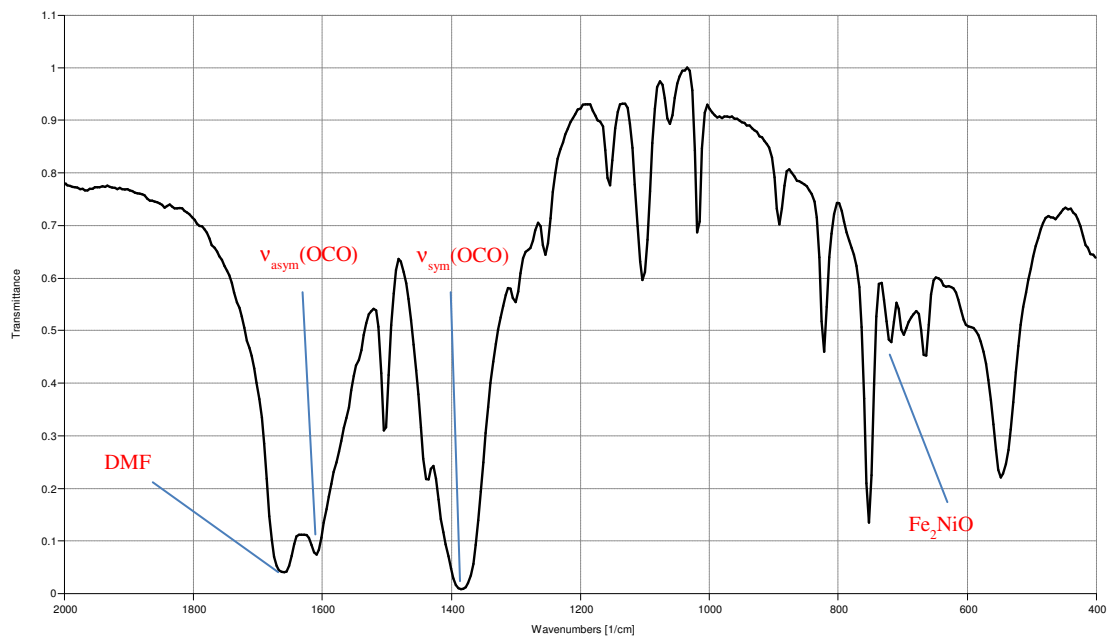


**Figure S1.** FTIR spectra of Fe$_2$Ni-MIL-88B.DMF
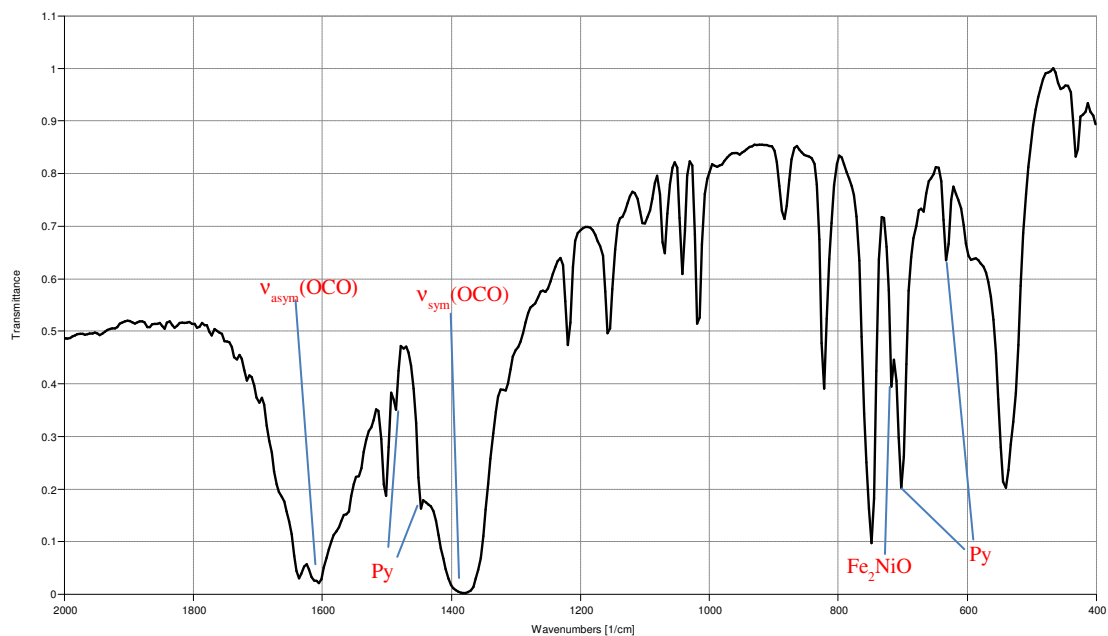


**Figure S2.** FTIR spectra of Fe$_2$Ni-MIL-88B.Py

3
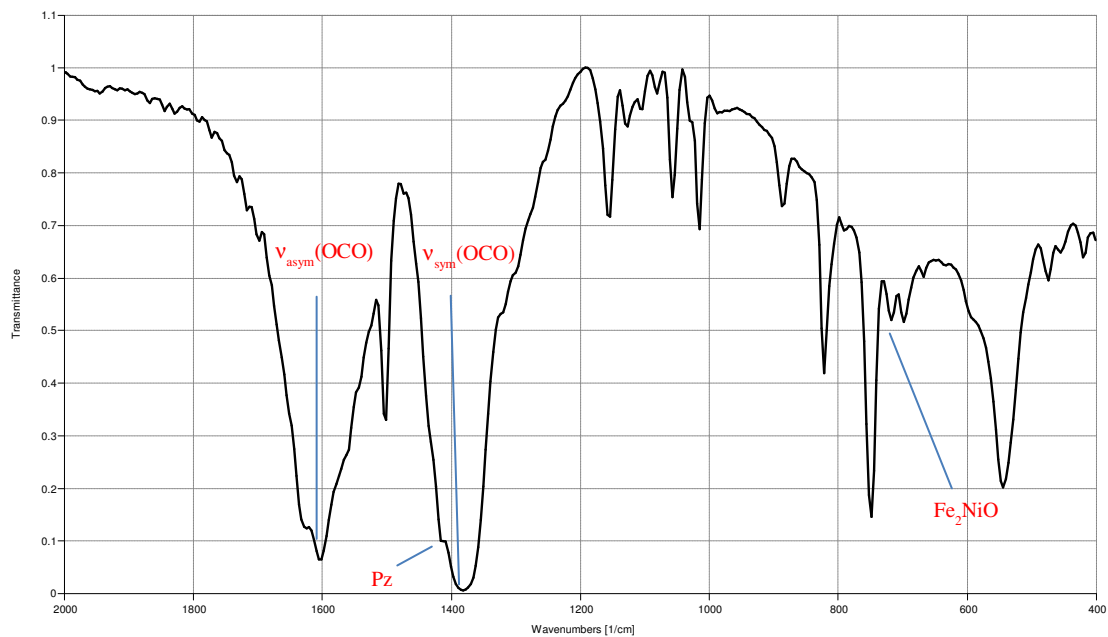
**Figure S3.** FTIR spectra of $Fe_2Ni$-MIL-88B.Pz
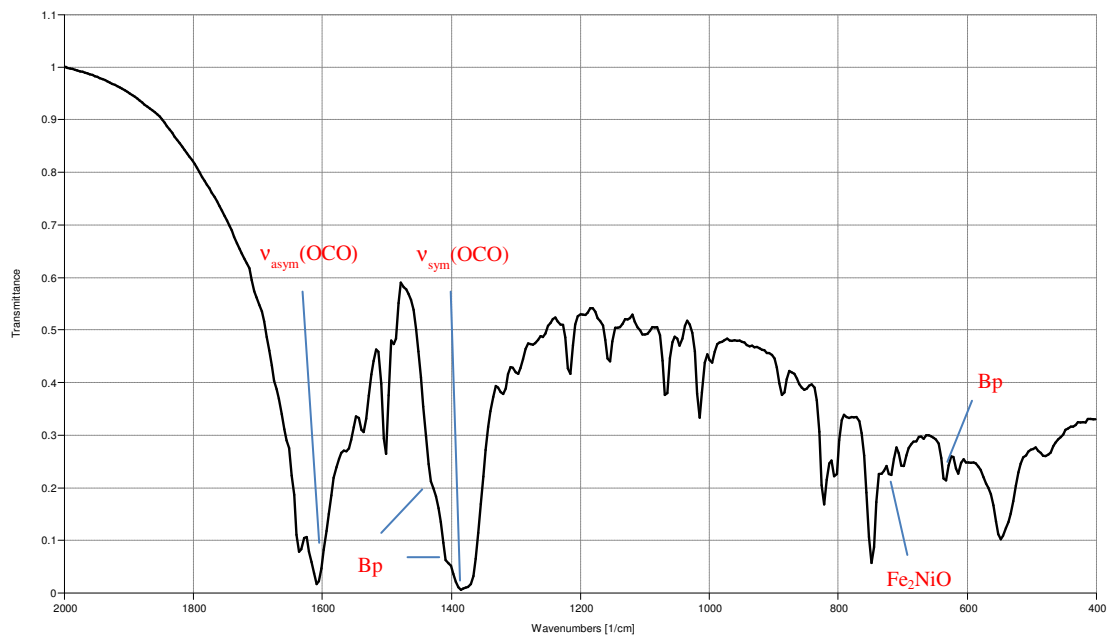


**Figure S4.** FTIR spectra of $Fe_2Ni$-MIL-88B.Bp
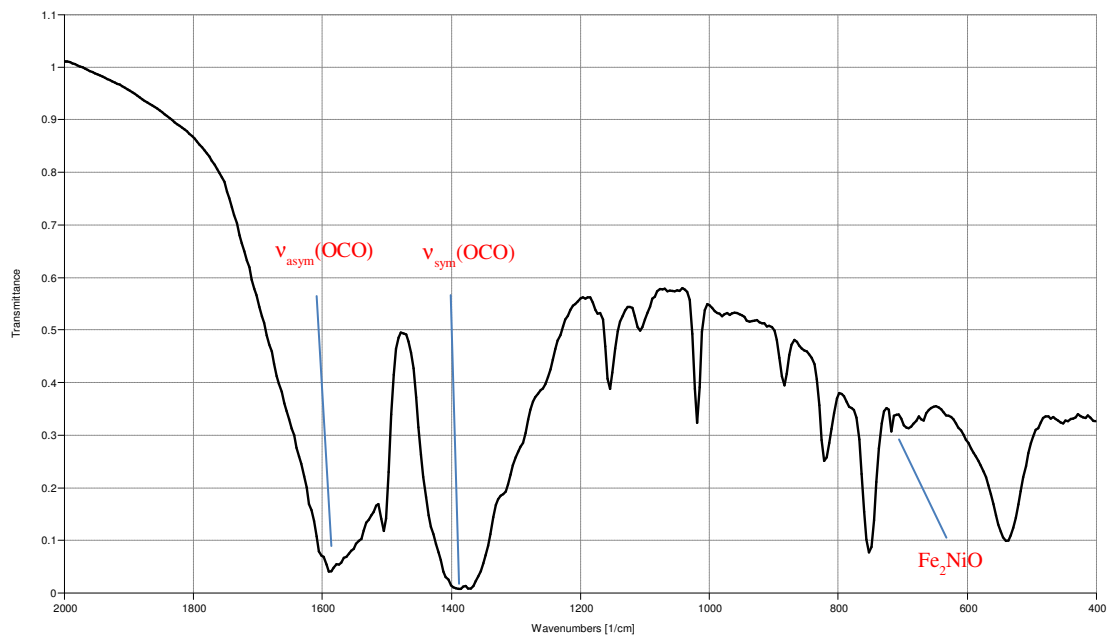
**Figure S5.** FTIR spectra of Fe$_2$Ni-MIL-88B.H$_2$O
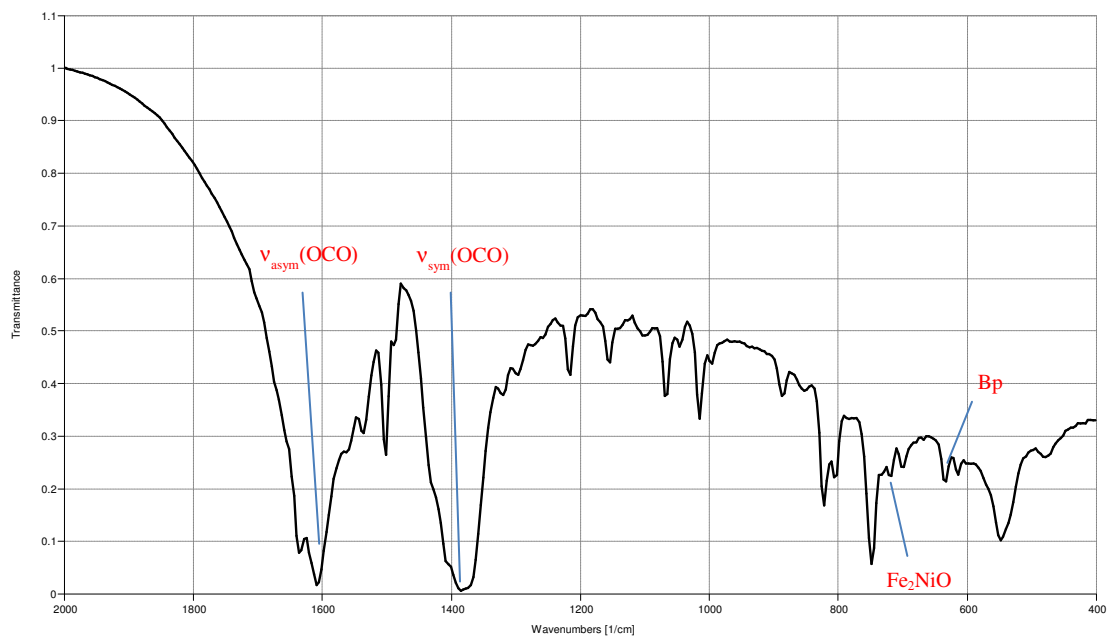
**Figure S6.** FTIR spectra of Fe$_3$-MIL-88B.DMF

5
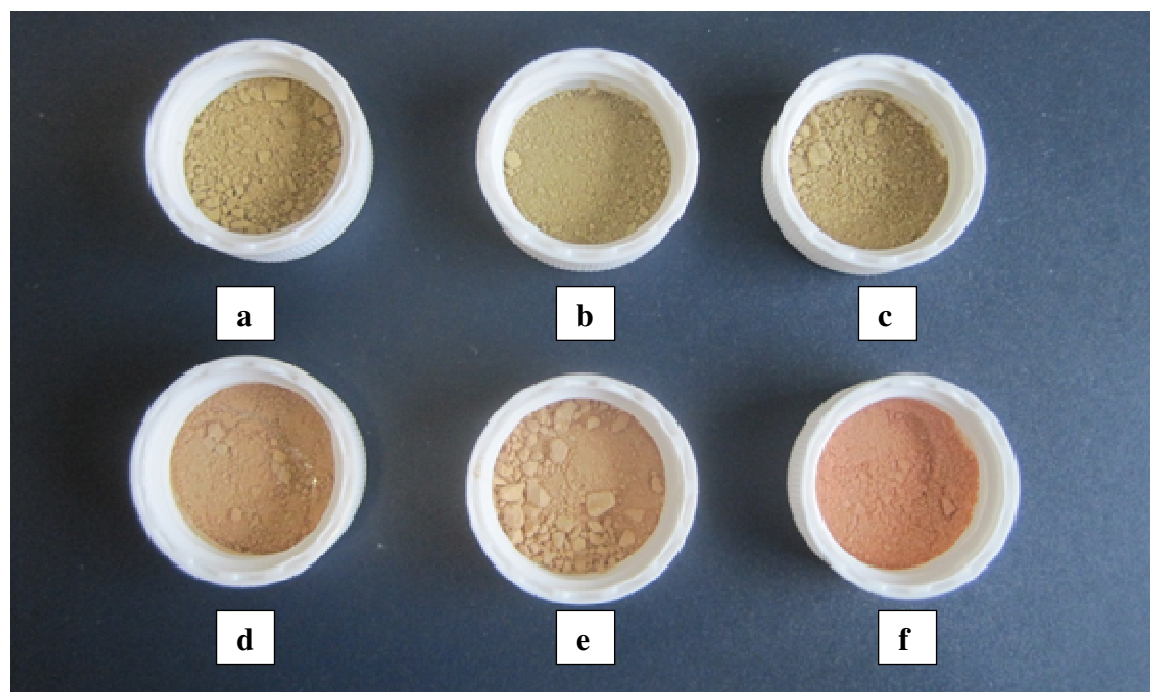
**Figure S7**. Images of $Fe_2Ni$-MIL-88B.Bp (a), $Fe_2Ni$-MIL-88B.Pz (b), $Fe_2Ni$-MIL-88B.Py (c), $Fe_2Ni$-MIL-88B.DMF (d) $Fe_2Ni$-MIL-88B.$H_2O$ (e) and Fe-MIL-88B.DMF (f).
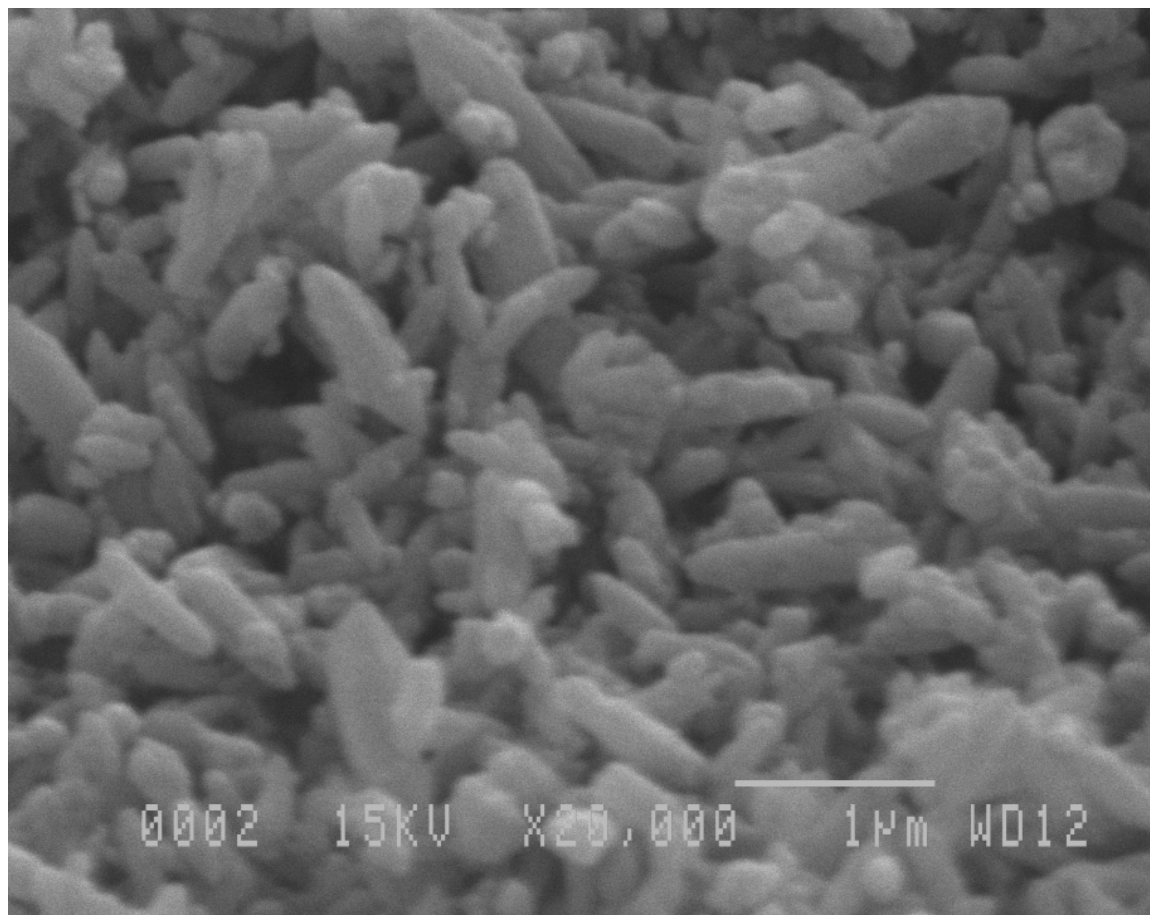
**Figure S8**. SEM image of as-synthesized $Fe_2Ni$-MIL-88B.DMF

**Ligand exchange reactions:**

+ DMF => $H_2O$: 0.25 g of $Fe_2Ni$-MIL-88B.DMF was added with 10 ml of water. The obtained mixture was stirred at room temperature for 3 hours, and then the solid was recovered by filtration and dried at 100 $^0$C overnight. XRD pattern showed in Figure 3e

+ $H_2O$=>DMF: 0.25 g of $Fe_2Ni$-MIL-88B.$H_2O$ was added with 10 ml of DMF. After stirring for 30 min, the mixture was transferred into an autoclave and it was placed in oven at 110 $^0$C for 3 days. The product was recovered by filtration and washed several times with DMF (Figure S9), BET specific surface area: 320 $m^2$/g.
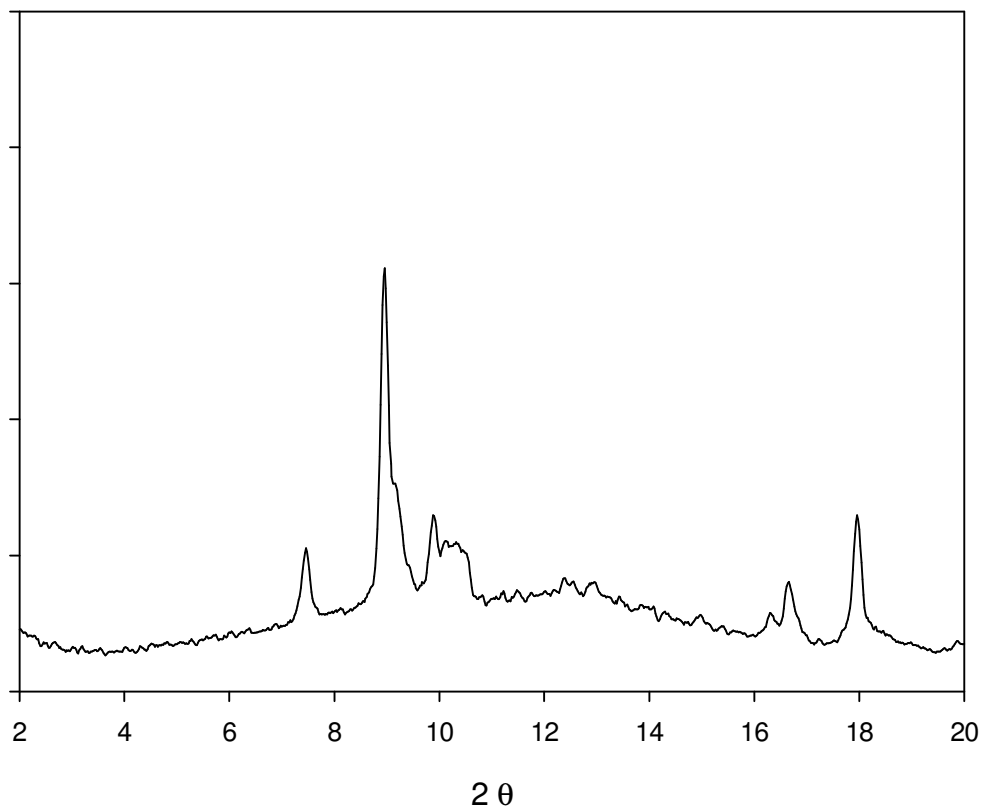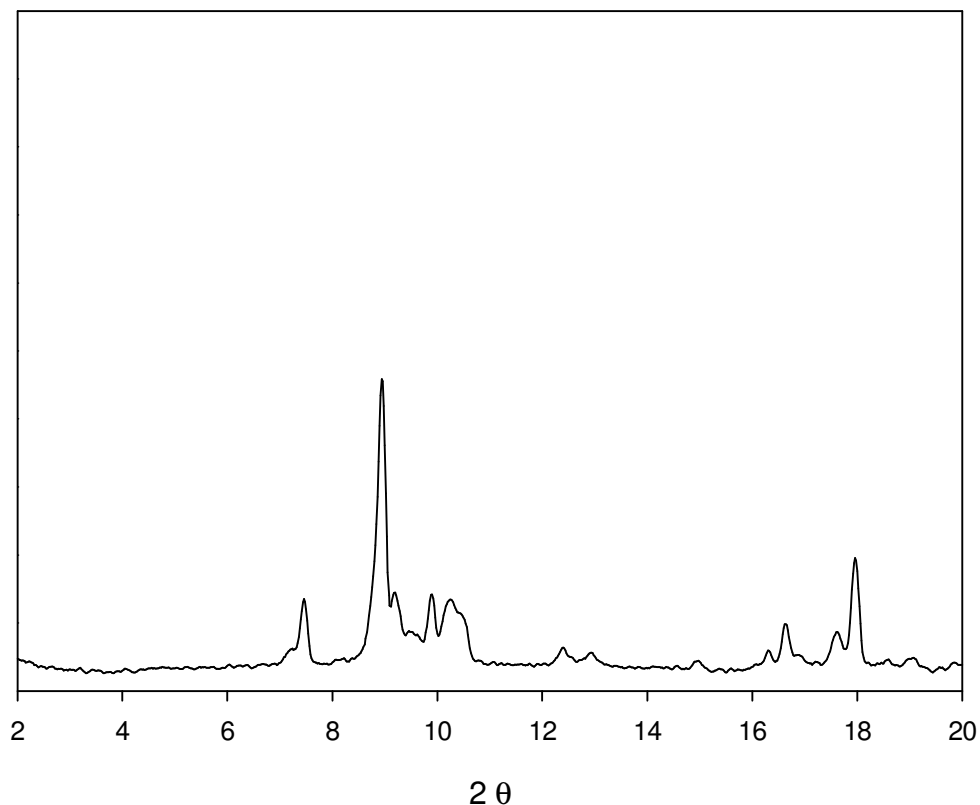


**Figure S9**: XRD pattern of $Fe_2Ni$-MIL-88B.DMF obtained from $Fe_2Ni$-MIL-88B.$H_2O$

+ DMF=>Py: 0.25 g of $Fe_2Ni$-MIL-88B.DMF was added with 10 g of pyridine. Very quickly the solid changed its color from brown to olive green. The mixture was stirred for 3 hours. The product was filtrated and dried in vacuum at 100 $^o$C overnight. XRD pattern showed in Figure 3c.

+ Py = > DMF. 0.25 g of $Fe_2Ni$-MIL-88B.Py was added with 10 ml of DMF. The mixture was stirred at 100 $^o$C for 3 days while the color gradually changed from olive green to yellow. The product was filtrated, washed with DMF and dried in vacuum at 100 $^o$C overnight (Figure S10). BET specific surface area: 340 $m^2$/g.



$2\theta$

**Figure S10**: XRD pattern of $Fe_2Ni$-MIL-88B.DMF obtained from $Fe_2Ni$-MIL-88B. Py

+ DMF = > Pz: 0.25 g of $Fe_2Ni$-MIL-88B.DMF was added with 10 g of pyrazine. The mixture was heated to 70 $^oC$ as pyrazine melted, stirring was applied for 3 hours. The olive green product was recovered by hot filtration and dried in vacuum at 100 $^oC$ overnight. XRD pattern showed in Figure 3b.

+ Pz => DMF: 0.25 g $Fe_2Ni$-MIL-88B.Pz was added with 10 ml of DMF, the mixture was transferred into an autoclave and heated at 100 $^oC$ for 3 days. Brown solid product was filtrated and washed with DMF before drying in vacuum at 100 $^oC$ overnight (Figure S11). BET specific surface area: 325 $m^2/g$.
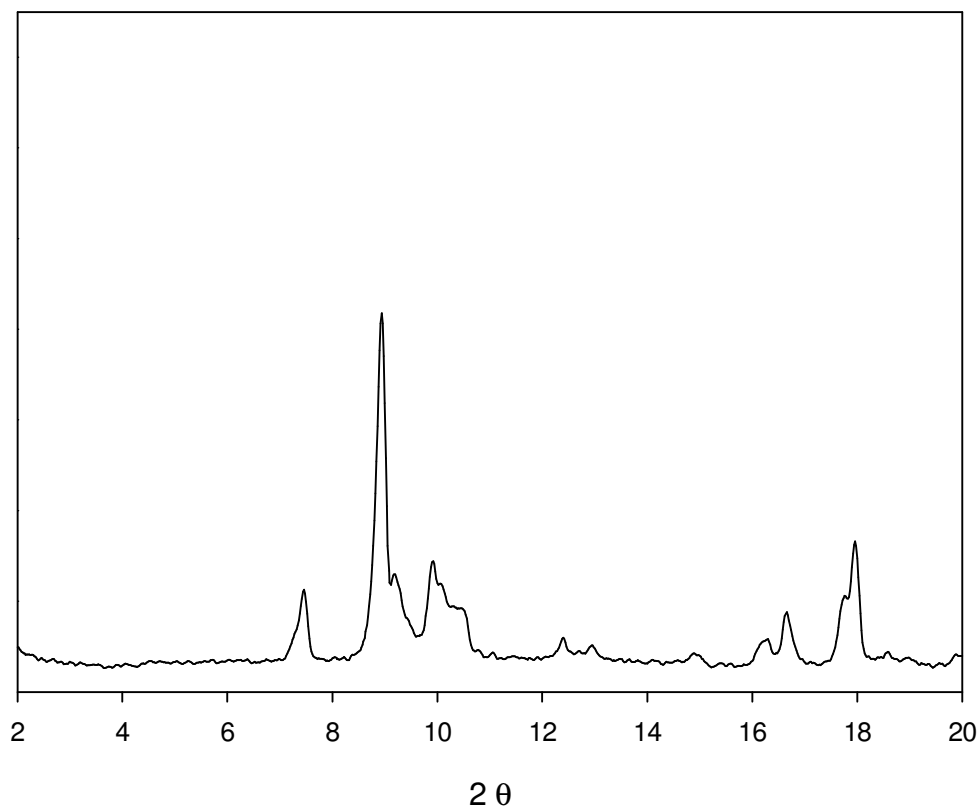


**Figure S11**: XRD pattern of $Fe_2Ni$-MIL-88B.DMF obtained from $Fe_2Ni$-MIL-88B. Pz

+ Pz = > $H_2O$: 0.25 of $Fe_2Ni$-MIL-88B.Pz in a vial was added with 15 ml of water. The vial was then sealed and stirred at 95 $^{o}C$. After 3 hours the brown product was filtrated and dried in vacuum at 100 $^{o}C$ overnight (Figure S12). BET specific surface area: 15 $m^2/g$.
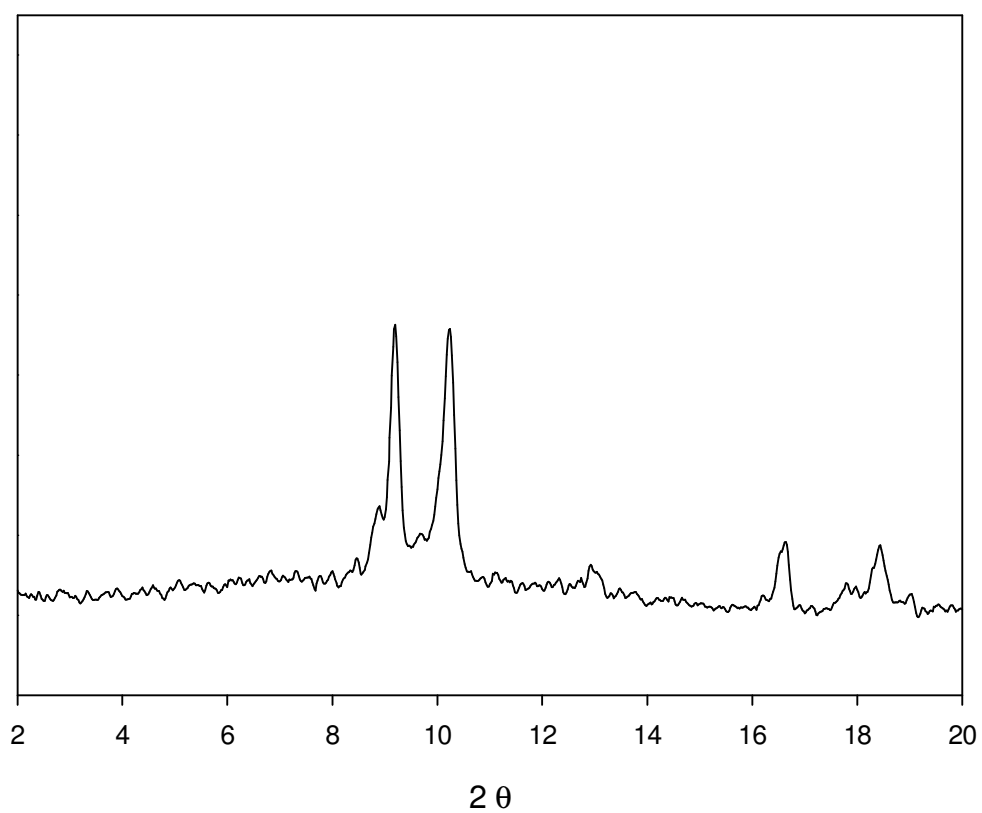


**Figure S12**: XRD pattern of $Fe_2Ni$-MIL-88B.$H_2O$ obtained from $Fe_2Ni$-MIL-88B. Pz

+ $H_2O$ => Pz: 0.25 g of $Fe_2Ni$-MIL-88B.$H_2O$ was added with 10 g of pyrazine. The mixture was heated at 100 $^o$C for 3 days. The olive green product was recovered by filtration and dried in vacuum at 100 $^o$C overnight (Figure S13). BET specific surface area: 420 m$^2$/g.
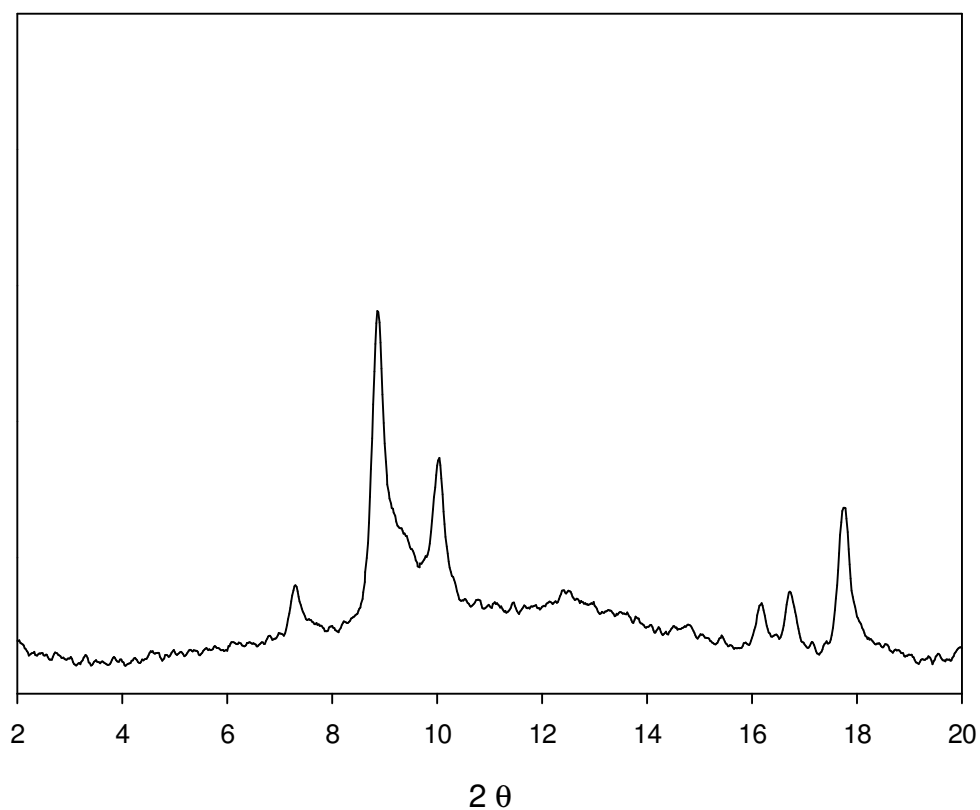


**Figure S13**: XRD pattern of $Fe_2Ni$-MIL-88B.Pz obtained from $Fe_2Ni$-MIL-88B. $H_2O$

+ Py => $H_2O$: 0.25 of $Fe_2Ni$-MIL-88B.Py in a vial was added with 15 ml of water. The vial was then sealed and stirred at 95 °C. After 3 hours the brown product was filtrated and dried in vacuum at 100 °C overnight (Figure S14), BET specific surface area: 10 $m^2$/g.
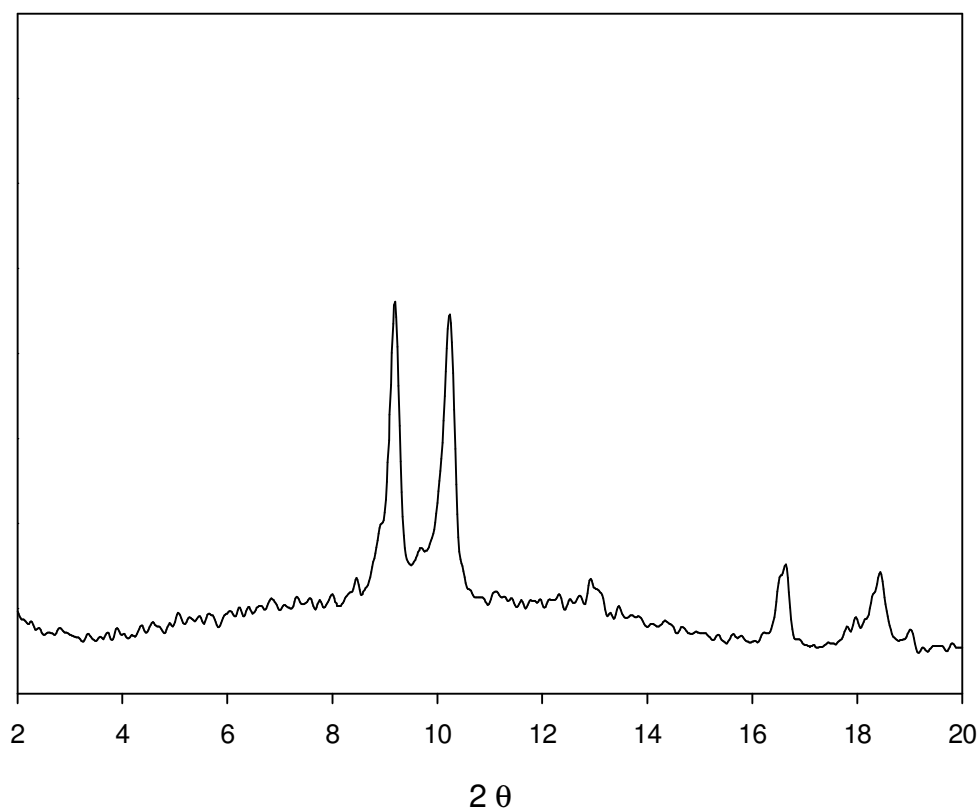


**Figure S14**: XRD pattern of $Fe_2Ni$-MIL-88B.$H_2O$ obtained from $Fe_2Ni$-MIL-88B. Py

+ $H_2O$ => Py: 0.25 g of $Fe_2Ni$-MIL-88B.$H_2O$ was added with 10 ml of pyridine. The mixture was sealed in a vial and stirred at 100 °C for 4 days. Olive green product was filtered and dried in vacuum at 100 °C overnight (Figure S14). BET specific surface area: 530 $m^2$/g
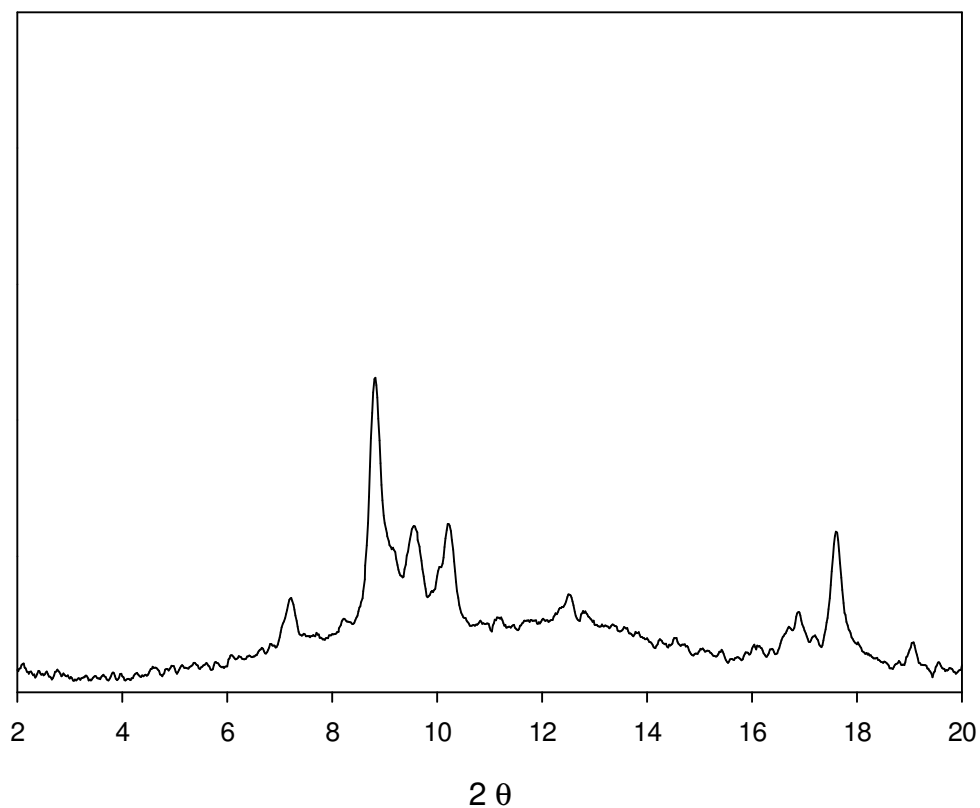
13

**Figure S15**: XRD pattern of $Fe_2Ni$-MIL-88B.Py obtained from $Fe_2Ni$-MIL-88B. $H_2O$

+ DMF => Bp: 0.16 g of bipyridine was introduced to 2 ml of DMF, to this solution 0.12 g of $Fe_2Ni$-MIL-88B.DMF was added. The mixture was then stirred at 100 $^o$C for 4 days. Olive green product was filtered and dried in vacuum at 100 $^o$C. XRD pattern showed in Figure 3a

+ Bp => DMF: 0.12 g of $Fe_2Ni$-MIL-88B.Bp was added with 15 ml of DMF, the mixture as transferred into an autoclave and it was placed in an oven at 100 $^o$C for 6 days. Brown product

was filtered and washed with DMF before drying in vacuum overnight at 100 $^{\circ}$C (Figure S16).
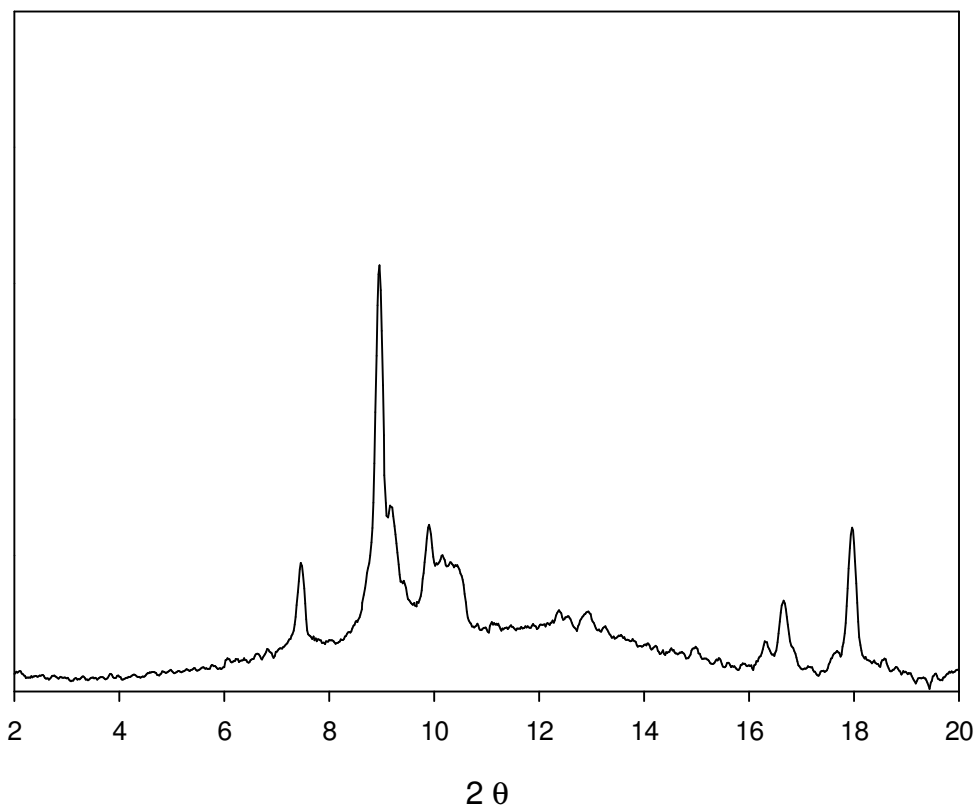
BET specific surface area: 330 m$^2$/g.



2 $\theta$

**Figure S16**: XRD pattern of Fe$_2$Ni-MIL-88B.DMF obtained from Fe$_2$Ni-MIL-88B.Bp

**References**

(1) S. Bauer, C. Serre, T. Devic, P. Horcajada, J. r. m. Marrot, G. r. Férey, N. Stock, *Inorg. Chem.*
**2008**, *47*, 7568